Using TDCP Measurements in a low-cost PPP-IMU hybridized filter for real-time applications

Anthony Guillard, Paul Thevenon, Carl Milner

Using TDCP Measurements in a low-cost PPP-IMU hybridized filter for real-time applications

Anthony Guillard, Paul Thevenon, Carl Milner *3D Aerospace, ENAC*

I. BIOGRAPHY

Anthony Guillard is a PhD student for ENAC and 3D Aeropace. His PhD aims at developing an innovative, low-cost PPP triple frequency algorithm and detecting multipath with machine learning techniques. Dr. Paul Thevenon obtained a PhD degree in the signal processing laboratory of ENAC in Toulouse, France. Since July 2013, he is employed by ENAC as Assistant Professor. His current activities are GNSS precise positioning, signal distortion monitoring and hybridization with other sensors. Carl Milner received his PhD from Imperial College London in 2009. He continues to work on satellite navigation applications within civil aviation as an assistant professor at ENAC.

Abstract

Much of the focus in current positioning systems is on high accuracy, oriented by developing powerful and computationally heavy algorithms; however, this approach is not compatible with systems that require real-time capabilities. Furthermore, most Precise Point Positioning (PPP) algorithms use ambiguity estimation techniques in order to leverage the precision of carrier phase measurements. We developed a low-cost PPP algorithm fused with an Inertial Measurement Unit that uses Time Differenced Carrier Phase (TDCP) measurements which remove the need to resolve the ambiguities while still benefiting from the most accurate Global Navigation Satellite System (GNSS) observables. To maximize the accuracy and continuity of the positioning solution, we designed a tightly coupled Extended Kalman Filter that is capable of processing triple frequency code, Doppler, and carrier phase or TDCP measurements. We observed that the filter which uses TDCP measurements performs 52% better than the solution with solely the code and Doppler measurements in deep urban conditions and 5% in open-sky conditions while taking 66% less computation time (in MATLAB) than the filter with carrier phase measurements. The results demonstrate that TDCP measurements are a solid alternative to carrier phase measurements, especially in deep urban conditions, for any computationally limited applications while maintaining a high level of accuracy.

II. INTRODUCTION

The main goal of this work is to present an alternative to carrier phase ambiguity estimation in Precise Point Positioning algorithms. Indeed, as the design of Precise Point Positioning algorithms has become more complex in an effort to maximize positioning accuracy, this approach presents a challenge for systems that require real-time capabilities with limited computational power or energy consumption.

Since, most Precise Point Positioning (PPP) algorithms use carrier phase ambiguity estimation techniques [Li, 2019] [Duong, 2019], the carrier phase ambiguity has to be dealt with to reap the accuracy benefit of these measurements. This mandatory process is often complicated and complexifies the positioning algorithms such as the LAMBDA method [Teunissen, 2006] which resolves the ambiguity or the Melbourne Wubbena Combination [Blewitt, 1990]. By estimating the ambiguity for each measurement in an Extended Kalman Filter, this augments the size of the state vector. However, the benefit of using carrier phase measurements, while keeping a low state vector size, can be obtained by using Time Differenced Carrier Phase (TDCP) measurements [Kim et al., 2020] [Soon et al., 2008] [Kai et al., 2021]. TDCPs are formed by differentiating two consecutive carrier phase observables which effectively removes the ambiguous term if no cycle slips are present.

To make the most of the TDCPs, an Extended Kalman Filter (presented in III.2) was designed. A low-cost inertial measurement unit was also used and tightly coupled in the filter to add robustness and continuity to the positioning solution. A cycle slip detection algorithm had also to be designed to exclude the corresponding affected TDCP measurements [Kim et al., 2020][Kai et al., 2021]. To assess the performance of the filter over the different datasets, a Novatel SPAN system was used as the reference trajectory.

Firstly, the article will present the approach taken to implement the filter, then the datasets will be presented. Finally, the results and conclusion will be discussed.

III. METHODOLOGY

1. Formation of Time Differenced Carrier Phase Measurements

Urban environments present the biggest challenge for GNSS-based positioning due to the large number of trees, metal posts, and buildings which in turn lead to more potential diffractions and reflections of the signals [Kaplan, 2017]. When these excess signals are processed by the receiver on top of the direct signal, this phenomenon is known as multipath interference. On the other hand, when the direct signal is masked by an obstacle and only the non-direct signals are processed by the receiver, this is known as a Non-Line-Of-Sight (NLOS) reception.

Both of these phenomena cause a positioning error because of the excess delay of the reflected/diffracted signals. It is shown in [Parkinson, 1996] that multipath errors in carrier phase measurements on GPS L1 do not exceed 4.8 cm while pseudorange errors can exceed 100 meters. Hence, since the carrier phase measurement is more robust to multipath, it is fitting to use it in urban conditions. The pseudorange and carrier phase models are given below.

$$\rho^i_{Rx} = (\vec{r^i} - \vec{r}_{Rx}) \cdot \vec{e_{Rx}}^{\,i} + c(dt_{Rx} - dt^i) + T^i_{Rx} + I^i_{Rx} + \delta^i_{\rho,Rx} + \varepsilon^i_{\rho,Rx} \tag{1}$$

$$\phi^i_{Rx} = (\vec{r^i} - \vec{r}_{Rx}) \cdot \vec{e_{Rx}}^{\,i} + c(dt_{Rx} - dt^i) + T^i_{Rx} - I^i_{Rx} + \lambda N^i_{Rx} + \delta^i_{\phi,Rx} + \varepsilon^i_{\phi,Rx} \tag{2}$$

Where:

- $\vec{r^i}$ is the satellite's position
- $\vec{r}_{Rx}$ is the receiver's position
- $\vec{e_{Rx}}^{\,i}$ is the line of sight (LOS) vector
- dt_{Rx} is the receiver clock error
- dt^i is the satellite clock error
- T^i_{Rx} is the Troposphere error
- I^i_{Rx} is the Ionosphere error
- λN^i_{Rx} is the ambiguity term
- $\delta^i_{obs,Rx}$ is the multipath of the given observable
- $\varepsilon^i_{obs,Rx}$ is the noise of the given observable
- ρ^i_{Rx} is the pseudorange
- ϕ^i_{Rx} is the carrier phase

The downside of carrier phase measurements is that they are ambiguous. To be used, their ambiguity term must be estimated. In a PPP algorithm, this is often done using an Extended Kalman Filter [Gao et al., 2017] [Vana et al., 2019]. However, these implementations are time and power consuming to have a precise estimate of the ambiguity factor due to the larger size of the state vector. Furthermore, when a cycle slip occurs, the algorithm must re-start the estimation process or repair the cycle slip [Bisnath, 2000] which may require a convergence period due to poor observability between the ambiguities and other states.

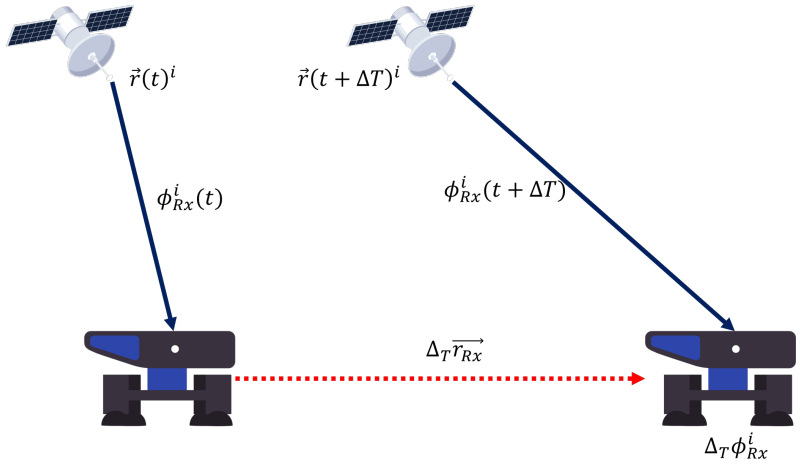

Figure 1: Formation of TDCP Measurements.

The time differenced carrier phase differentiates two consecutive carrier phase measurements to effectively eliminate the ambiguity term in the absence of cycle slips as shown in figure 1. Thus, the TDCP still uses the precision of the carrier phase measurement while keeping a low implementation complexity. Indeed, only a cycle slip detector must be implemented but with no re-convergence period needed and a lower state vector size. The TDCP can be obtained as follows:

$$\Delta_T\phi^i_{Rx} = \phi^i_{Rx}(t+\Delta T) - \phi^i_{Rx}(t) \tag{3}$$

$$\begin{aligned}\Delta_T\phi^i_{Rx} = (\vec{r}^i(t+\Delta T) - \vec{r}_{Rx}(t+\Delta T)) \cdot \vec{e_{Rx}}^i(t+\Delta T) - (\vec{r}^i(t) - \vec{r}_{Rx}(t)) \cdot \vec{e_{Rx}}^i(t) \\ +\Delta_T(cdt_{Rx}) - \Delta_T(cdt^i) + \Delta_T T^i_{Rx} + \Delta_T I^i_{Rx} + \Delta_T\delta^i_{\phi,Rx} + \Delta_T\varepsilon^i_{\phi,Rx}\end{aligned} \tag{4}$$

As long as Δ_T is not too big, the tropospheric, ionospheric, and multipath temporal evolutions are considered to be negligible [Park and Kee, 2010]. These error sources are included in the TDCP residual noise term ($\Delta_T E^i_{Rx}$).

$$\begin{aligned}\Delta_T\phi^i_{Rx} = \vec{r}^i(t+\Delta_T) \cdot \vec{e_{Rx}}^i(t+\Delta_T) - \vec{r}^i(t) \cdot \vec{e_{Rx}}^i(t) - \Delta_T\vec{r}_{Rx} \cdot \vec{e_{Rx}}^i(t+\Delta_T) - \\ \vec{r}_{Rx}(t)\Delta_T \cdot \vec{e_{Rx}}^i + \Delta_T(cdt_{Rx}) - \Delta_T(cdt^i) + \Delta_T E^i_{Rx}\end{aligned} \tag{5}$$

Where $\Delta_T E^i_{Rx} = \Delta_T T^i_{Rx} + \Delta_T I^i_{Rx} + \Delta_T\delta^i_{\phi,Rx} + \Delta_T\varepsilon^i_{\phi,Rx}$ represents the temporal change of GNSS errors as well as the noise.

2. Extended Kalman Filter

To use the TDCPs, on top of the pseudoranges and Dopplers, an error state Extended Kalman Filter was designed. The Inertial Navigation Solution (INS) is the reference solution and the GNSS observables are used as the measurements for the EKF updates. In order to quantify the added value of TDCPs with respect to the traditional method, the possibility of using carrier phase measurements in the filter was also added. When the filter uses solely pseudoranges and Doppler measurements with or without TDCP measurements the estimated states are:

$$\delta X_k = [\delta r^e_k \;\; \delta v^e_k \;\; \delta\psi^e_k \;\; \delta dt_{Rx_k} \;\; \delta\dot{dt}_{Rx_k} \;\; \delta dt_{GPS-GAL,k} \;\; \delta b_{acc_k} \;\; \delta b_{gyro_k} \;\; \delta ztd_k] \tag{6}$$

This filter estimates the errors of the receiver position, velocity, attitude (in the Earth Centered Earth Fixed frame [Zhu, 1994]), clock bias, clock drift, inter-system bias between GPS and Galileo, the IMU's accelerometer and gyroscope biases, and the zenith tropospheric delay respectively. While when the filter uses carrier phase measurements, the state vector adds more states which correspond to the ambiguity for each measurement.

$$\delta X_k = [\delta r^e_k \;\; \delta v^e_k \;\; \delta\psi^e_k \;\; \delta dt_{Rx_k} \;\; \delta\dot{dt}_{Rx_k} \;\; \delta dt_{GPS-GAL,k} \;\; \delta b_{acc_k} \;\; \delta b_{gyro_k} \;\; \delta ztd_k \;\; \delta N_1 \ldots \delta N_n] \tag{7}$$

The nominal process and measurement models for the Extended Kalman Filter are given below [Groves, 2008]:

$$\begin{aligned} X_k &= \Phi_{k-1} X_{k-1} + w_{k-1} \\ Z_k &= H_k X_k + v_k \end{aligned} \tag{8}$$

The state transition matrix, Φ_{k-1}, is equal to:

$$\Phi_{k-1} = \begin{bmatrix} I_3 & \Delta_T I_3 & 0_3 & 0 & 0 & 0 & 0_3 & 0_3 & 0 \\ 0_3 & I_3 - 2\Omega_{ie}\Delta_T & [-R_b^e f^b \times]\Delta_T & 0 & 0 & 0 & -R_b^e R_{imu}^b \Delta_T & 0_3 & 0 \\ 0_3 & 0_3 & I_3 - \Omega_{ie}\Delta_T & 0 & 0 & 0 & 0_3 & -R_b^e R_{imu}^b \frac{\pi}{180}\Delta_T & 0 \\ 0_{1\times3} & 0_{1\times3} & 0_{1\times3} & 1 & \Delta_T & 0 & 0_{1\times3} & 0_{1\times3} & 0 \\ 0_{1\times3} & 0_{1\times3} & 0_{1\times3} & 0 & 1 & 0 & 0_{1\times3} & 0_{1\times3} & 0 \\ 0_{1\times3} & 0_{1\times3} & 0_{1\times3} & 0 & 0 & 1 & 0_{1\times3} & 0_{1\times3} & 0 \\ 0_3 & 0_3 & 0_3 & 0 & 0 & 0 & I_3 & 0_3 & 0 \\ 0_3 & 0_3 & 0_3 & 0 & 0 & 0 & 0_3 & I_3 & 0 \\ 0_3 & 0_3 & 0_3 & 0 & 0 & 0 & 0_3 & 0_3 & 1 \end{bmatrix} \tag{9}$$

Where:

- R_{imu}^b is the rotation matrix from the IMU's frame to the body frame
- R_b^e is the rotation matrix from the body frame to the ECEF
- f^b is the accelerometer reading rotated to the body frame with respect to the inertial frame
- ω^b is the gyrometer reading rotated to the body frame with respect to the inertial frame
- $[v\times]$ denotes the skew matrix of the vector in brackets which is equal to: $\begin{bmatrix} 0 & -v_3 & v_2 \\ v_3 & 0 & -v_1 \\ -v_2 & v_1 & 0 \end{bmatrix}$
- $\Omega_{ie} = \begin{bmatrix} 0 & -\omega_{ie} & 0 \\ \omega_{ie} & 0 & 0 \\ 0 & 0 & 0 \end{bmatrix}$ with $\omega_{ie} = 7.292115 \times 10^{-5}$ rad/s being the WGS84 Earth's angular rate
- I_N is the identity matrix of size N
- $0_{N\times M}$ is a zero matrix of size [N, M]

H_k depends on the observation being processed. For pseudoranges and Dopplers, the measurement matrix is well known.For TDCP measurements, it is defined as:

$$H_{k,TDCP} = \begin{bmatrix} -\vec{e_{Rx}}^i(t) & \vec{e_{Rx}}^i(t) - \vec{e_{Rx}}^i(t - \Delta T) & -\vec{e_{Rx}}^i(t) R_e^b(t) & 1 & 0 & \dots & 0 \end{bmatrix} \tag{10}$$

In this project, as for most, it is assumed that the state process noise and measurement noise are not correlated in time, yielding:

$$\begin{aligned} E[w_{k_i} w_{k_j}^T] &= \begin{cases} Q_k, & \text{iif } k_i = k_j \\ 0, & \text{otherwise} \end{cases} \\ E[v_{k_i} v_{k_j}^T] &= \begin{cases} R_k, & \text{iif } k_i = k_j \\ 0, & \text{otherwise} \end{cases} \end{aligned} \tag{11}$$

This is assumed because the noise of the measurements is assumed to be white Gaussian noise and the same goes for the state process noise.

The measurement noise matrix R_k can be defined as:

$$R_k = \begin{bmatrix} \sigma_{obs}^2 \end{bmatrix} \tag{12}$$

Where σ_{obs} is the standard deviation of the measurement being processed. As the filter deals with measurements sequentially, R_k is of size 1×1.

The state covariance matrix Q_k is defined as:

$$Q_k = \begin{bmatrix} 0_3 & 0_3 & 0_3 & 0 & 0 & 0 & 0_3 & 0_3 & 0 \\ 0_3 & Q_{vel} & 0_3 & 0 & 0 & 0 & 0_3 & 0_3 & 0 \\ 0_3 & 0_3 & Q_{att} & 0 & 0 & 0 & 0_3 & 0_3 & 0 \\ 0_{1\times3} & 0_{1\times3} & 0_{1\times3} & 0 & 0 & 0 & 0_{1\times3} & 0_{1\times3} & 0 \\ 0_{1\times3} & 0_{1\times3} & 0_{1\times3} & 0 & Q_{rxDrift} & 0 & 0_{1\times3} & 0_{1\times3} & 0 \\ 0_{1\times3} & 0_{1\times3} & 0_{1\times3} & 0 & 0 & Q_{interGnss} & 0_{1\times3} & 0_{1\times3} & 0 \\ 0_3 & 0_3 & 0_3 & 0 & 0 & 0 & Q_{acc} & 0_3 & 0 \\ 0_3 & 0_3 & 0_3 & 0 & 0 & 0 & 0_3 & Q_{gyro} & 0 \\ 0_3 & 0_3 & 0_3 & 0 & 0 & 0 & 0_3 & 0_3 & Q_{Tropo} \end{bmatrix} \tag{13}$$

Where the Q_{state} matrices are equal to the variance of the state noise multiplied by the state refresh rate (so the rate of the IMU).

The incorporation of the TDCP measurements throws off this assumption as these observables are obtained from positions of different time epochs (current and past) [Brown, 2012]. Rewriting Equation 8, this gives:

$$X_{k-1} = \Phi_{k-1}^{-1} X_k - \Phi_{k-1}^{-1} w_{k-1} \tag{14}$$

The measurement model must be rewritten as a function of the current and previous states:

$$Z_k = H_k X_k + J_k X_{k-1} + v_k \tag{15}$$

Where $J_k = -H_k$. By plugging equation 14 into equation 15, the new measurement model is given as:

$$Z_k^{'} = (H_k + J_k \Phi_{k-1}^{-1}) X_k + (-J_k \Phi_{k-1}^{-1} w_{k-1} + v_k) \tag{16}$$

Since R_k is given by the correlation of v_k, the updated measurement noise matrix is given by:

$$R_k^{'} = E\left[(-J_k \Phi_{k-1}^{-1} w_{k-1} + v_k)(-J_k \Phi_{k-1}^{-1} w_{k-1} + v_k)^T\right] \tag{17}$$

After simplification, this equals to:

$$R_k^{'} = R_k + J_k \Phi_{k-1}^{-1} Q_{k-1} {\Phi_{k-1}^{-1}}^T J_k^T \tag{18}$$

This also has repercussions on the Kalman Gain and state covariance matrix update steps, with the new formulas given below:

$$K_k^{'} = (P_k^- H_k^T + \Phi_{k-1} P_{k-1} J_k^T)(H_k P_k^- H_k^T + R_k + J_k P_{k-1} \Phi_{k-1}^T H_k^T + H_k \Phi_{k-1} P_{k-1} J_k^T + J_k P_{k-1} J_k^T)^{-1} \tag{19}$$

$$P_k = P_k^- - K_k L_k K_k^T \tag{20}$$

Where $L_k = (H_k P_k^- H_k^T + R_k + J_k P_{k-1} \Phi_{k-1}^T H_k^T + H_k \Phi_{k-1} P_{k-1} J_k^T + J_k P_{k-1} J_k^T)$.

Since the equations for the measurement update are different for TDCPs, the Extended Kalman Filter was designed so that the measurements were treated sequentially [Welch and Bishop, 1997]. This also leads to a smaller computational burden as finding the inverse of a NxM (with $N, M \in \mathbb{N} \setminus \{0, 1\}$) matrix is never computed except for the state transition matrix, Φ_{k-1}^{-1}, but is a constant if the timings between two consecutive measurements is the same [Groves, 2008]. The other benefit is that the filter can have two sets of measurement update equations depending on the observable treated at a given instant: one for TDCPs and the other set for code and Doppler measurements.

TDCPs are constructed by the difference of two consecutive carrier phase measurements, two consecutive TDCPs use the same carrier phase measurement as highlighted in the following equation.

$$\begin{aligned} \Delta_T \phi_{Rx}^i(t) &= \phi_{Rx}^i(t) - \phi_{Rx}^i(t - \Delta T) \\ \Delta_T \phi_{Rx}^i(t + \Delta T) &= \phi_{Rx}^i(t + \Delta T) - \phi_{Rx}^i(t) \end{aligned} \tag{21}$$

Hence, two consecutive TDCPs are correlated. If one wants to use consecutive time differenced carrier phase measurements, an extra state must be added in the filter to account for the correlation. In the proposed implementation, another solution was

chosen: performing the TDCP measurement update once every two epochs. Although, the potential benefit of using TDCP every epoch is lost, it results in a decorrelation of the measurements, a simpler implementation, and saves computational power.

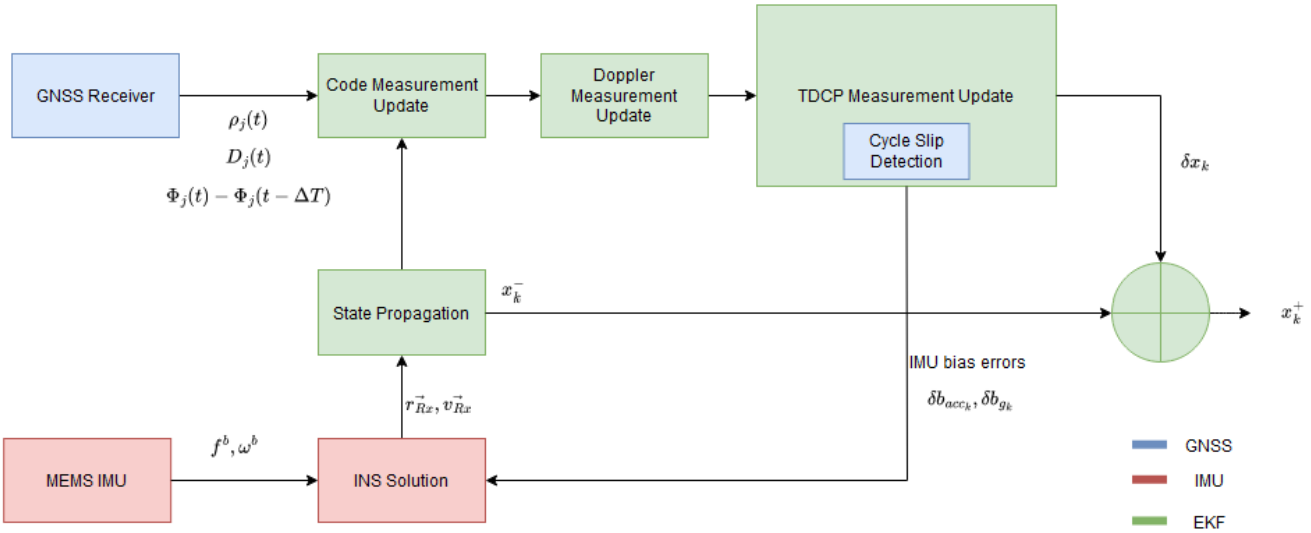

Figure 2: EKF Filter Architecture for one epoch.

3. Cycle Slip Detection

As mentioned earlier and highlighted by equation 3, the ambiguous term present in carrier phase measurements is absent of TDCPs under one condition: no cycle slips occur during the interval of time. If a cycle slip occurs during this time interval, equation 3 can be re-written as:

$$\Delta_T \phi^i_{Rx} = \phi^i_{Rx}(t + \Delta T) - \phi^i_{Rx}(t) + \Delta N \lambda \tag{22}$$

The TDCP filter does not estimate the ambiguity nor does it try to estimate the ambiguity change, so ideally the cycle slip affected TDCP should be discarded by the filter. To do so, two methods are implemented in the filter:

- EKF rejection based on the innovations and their covariance [Tanil, 2022]
- Threshold comparison between the wavelength of the signal and the expected observation noise of the innovation [Kim et al., 2020]

The benefit of both of these implementations is that there are no combinations of signals used unlike cycle slip detection when using carrier phase measurements [Kim and Langley, 2001].

a) EKF based Cycle Slip Rejection

The EKF rejection is not specifically made to detect cycle slips but rather to monitor the innovations and exclude abnormally large innovations. Cycle slips can produce large innovations for TDCPs that exceed a threshold determined based on the expected measurement noise, given in equation 18. First the innovation covariance is computed:

$$I_{k,cov} = (H_k + J_k \Phi^{-1}_{k-1}) P^-_{k-1} (H_k + J_k \Phi^{-1}_{k-1})^T \tag{23}$$

The innovations are normalized by the innovation covariance and then squared, resulting in the metric to be compared to a given threshold as given by [Tanil, 2022]:

$$M = I_k^T I^{-1}_{k,cov} I_k \tag{24}$$

M has a chi square distribution with a number of degree of freedom equal to the number of measurements processed. As the presented filter processes measurements sequentially, it equals one in this case. The selection of the threshold depends on the desired sensitivity vs false alarm rate. In this project, the threshold is obtained by fixing a measurement rejection rate as follows:

$$T = Inv - \chi^2(1 - P_{EKF_{rej}}) \tag{25}$$

Where $P_{EKF_{rej}}$ is the desired probability at which the filter rejects a measurement.
Finally, the decision to exclude or not the measurement was made as such:

$$\text{Decision} = \begin{cases} M \geq T \rightarrow \text{Reject measurement} \\ M < T \rightarrow \text{Accept Measurement} \end{cases} \tag{26}$$

b) Wavelength based Cycle Slip Rejection

This method is a slightly modified version of the algorithm proposed in [Du and Gao, 2012] as they were using double differenced TDCPs which influenced their noise model. The smallest cycle slip that can exist in (22) is $\Delta N = 1$. So, the detector should be able to detect a change superior or equal to the wavelength of the processed signal (or signals if using iono-free TDCPs).

Equation 5 is re-used but also adding the cycle slip to the measurement. Then by using the predicted TDCP measurement from the filter, the two measurements are differenced (which is also the innovation). This yields:

$$M = \Delta_T \phi^i_{Rx} - \Delta_T \phi^i_{INS} \tag{27}$$

To detect a cycle slip, the terms other than the displacement of the receiver affecting M must be accounted for. The difference between the predicted and observed satellite and receiver clock drift must be small.

With the variance of M being:

$$\sigma^2_M = \text{var}(\Delta_T c\dot{dt}_{Rx}) + \text{var}(\Delta_T \vec{r}_{Rx_{INS}}) + \sigma^2_{\Delta_T E} \tag{28}$$

Where $\text{var}(\Delta_T c\dot{dt}_{Rx})$, $\text{var}(\Delta_T \vec{r}_{Rx_{INS}})$, $\sigma^2_{\Delta_T E}$, and σ^2_M are the variance of the clock drift difference, the variance of the IMU's positioning error, the variance of the remaining errors, and the variance of the metric M respectively.

To decide whether a cycle slip occurs, a Neyman-Pearson (NP) test is implemented. A NP test makes two hypotheses [Neyman and Pearson, 1933]:

- H_0: No Cycle slip occurs, there is only noise.
- H_1: A Cycle slip occurs: there is noise and at least a change of one wavelength.

The detection threshold can then computed as:

$$T = \lambda \tag{29}$$

Where λ is the wavelength of the signal.

The hypothesis H_0 can be modeled as a centered chi squared distribution, as the variance of M is a sum of Gaussian variables [Rahman et al., 2015]. On the other hand, the hypothesis H_1 can be also be modeled as a chi squared distribution but with a non-centrality parameter that is equal to λ.

The decision on the cycle slip presence is given as follows:

$$\text{Decision} = \begin{cases} M \geq T \rightarrow \text{Reject measurement} \\ M < T \rightarrow \text{Accept Measurement} \end{cases} \tag{30}$$

In a NP test, there are four distinguishable cases shown in Table 1.

Truth \ Expected	H_0	H_1
H_0	P_N	P_{Fa}
H_1	P_{Md}	P_D

Table 1: Neyman-Pearson Test Probabilities

Where:

- P_N is the probability of not detecting a cycle slip when there is none
- P_{Fa} is the probability of detecting a cycle slip when there is none

- P_{Md} is the probability of not detecting a cycle slip when there is one
- P_D is the probability of detecting a cycle slip when there is one

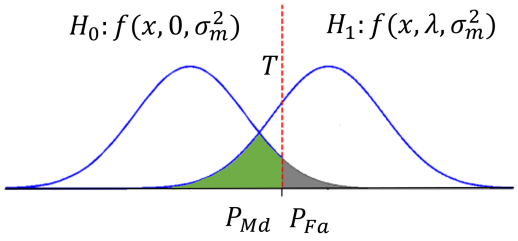

Figure 3: Neyman-Pearson Test for cycle slips.

As illustrated by figure 3 and table 1, there is a trade-off between a low missed detection and a low false alarm probability. A false alarm in this case will reduce the TDCP measurement availability as it will be excluded from the EKF process whereas a missed detection will result in a cycle slip being processed in the EKF.

IV. DATASETS

The filter was run on several datasets that were collected either using IGS data from the TLSE reference station or using a vehicle in Toulouse, France (in different environments). Dynamic datasets include an open sky highway scenario with few bridges, a mid-urban environment, and a deep urban scenario. On the other hand, the IGS data is collected in an open-sky environment and has triple frequency observables. The precise clock and orbit products (rapid), and phase center offset files were also downloaded and used in the filter's navigation solution to emulate a real-time PPP solution.

IGS Dataset

The IGS dataset was also a tool to verify that the filter was performing up to par. Indeed, the IGS station is in open sky environment and static with a geodetic antenna. The GNSS receiver used to generate the observables is the Trimble NETR9. This dataset also enabled us to test and implement the triple frequency combinations (Galileo E1 + Galileo E5a + Galileo E5b). Due to the lack of INS data from this IGS station, this version of the EKF filter was implemented in GNSS-only. The observables were available at a rate of 1Hz and gathered on the 4th of October 2021 for a duration of one hour. The reference position of the IGS TLSE station is given by the IGS website.

Dynamic Datasets

The dynamic datasets were all obtained with the same equipment. A uBlox active patch antenna was used and connected to a uBlox F9P receiver generating the measurements at a rate of 5Hz. The Inertial Measurement Unit (IMU) used is a low-cost Micro-electromechanical systems (MEMS), the Bosch BMI160 at a rate of 200Hz. The GNSS observables are obtained on Galileo (E1b + E5b) and GPS (L1 C/A + L2).

a) Reference Trajectory

The SPAN reference system consists of a high-performance IMU and a GNSS receiver. In post processing with Novatel's Inertial Explorer software, inertial and GNSS observations are combined in a forward-backward smoother. The SPAN GNSS receiver tracks all current constellations whose observations were used in post processing to obtain a more accurate reference trajectory.

b) Differences between Datasets

To quantify the benefit of using TDCP measurements, several environments had to be explored in the datasets. Hence, as mentioned earlier, there is an open sky highway scenario with few bridges, a mid-urban environment, and a deep urban scenario. The dates and duration of each scenario is given below:

- 29th of October 2020: Mid-Urban of 25 minutes
- 23rd of April 2021: Deep Urban of 15 minutes

- 21st of September 2021: Highway with few bridges of 54 minutes

V. RESULTS

This section is divided into two subsections: the IGS dataset and the dynamic data collects. The first results presented are from the IGS data collect to both explore the addition of TDCPs in a static and open sky environment. This also serves to demonstrate the performance of the presented filter in "ideal" conditions. The second part of the results are for the dynamic datasets which highlight the benefit of using TDCP measurements in different scenarios. The TDCP filter will be evaluated by using either uncombined TDCPs or first order iono-free ones. Both types of measurements will be tested by the cycle slip rejection algorithms – the EKF based rejection and the wavelength methods.

The results presented in this section will show different implementations of the filter that process different measurements:

- v2: Uses Code + Doppler measurements in the EKF measurement update, with the states of equation 6
- v3TDCP: Uses Code + Doppler + TDCP measurements in the EKF measurement update, with the states of equation 6
- v3: Uses Code + Doppler + Carrier phase measurements in the EKF measurement update, with the states of equation 7

1. IGS Dataset

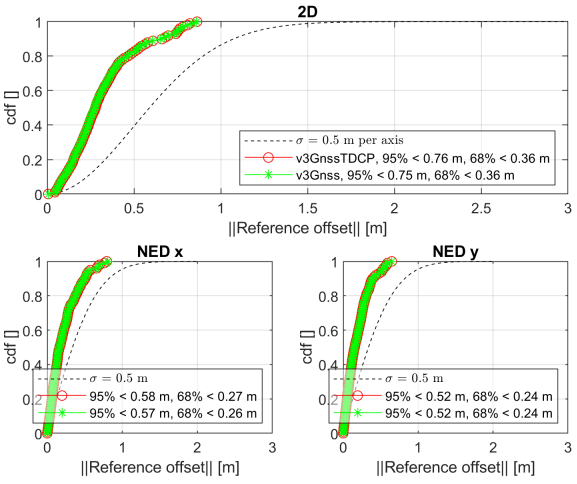

Figure 4: IGS CDFs.

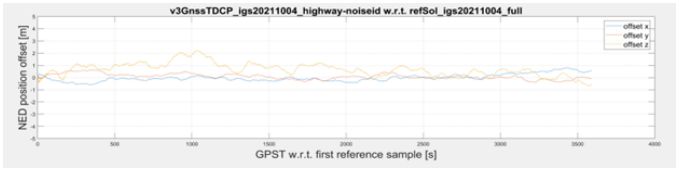

Figure 5: IGS time series v3TDCP.

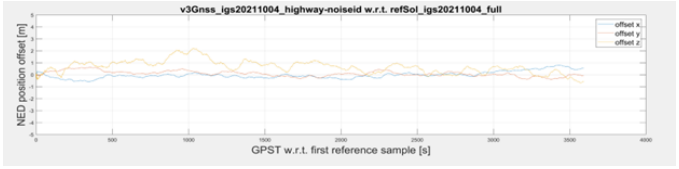

Figure 6: IGS time series v3.

Figures 5 and 6 depict the estimated position with respect to the reference in the North East Down (NED) coordinate frame as a function of time for the TDCP and ambiguity estimation filter respectively. Figure 4 shows the Cumulative Distribution Function (CDF) of the position error in meters for the x and y axes of the NED (north and east). This batch of results was generated using Dual Frequency observables on GPS (L1 C/A and L2) and Galileo (E1b + E5b) that were combined to remove the first order Ionospheric term. Both filters display relatively low positioning error and validate the proposed implementation. However, the benefit of TDCP measurements in a static environment seems to be non-existent as the performance of the TDCP filter is equal to the one without its inclusion (v2). This is not surprising as the TDCP estimates the distance between two consecutive epochs. As there is no distance being traveled, the code and Doppler take over the precision of the filter.

	v2	v3	v3$_{TDCP_{IF}, I_{rej}}$	v3$_{TDCP_{Unc}, I_{rej}}$	v3$_{TDCP_{IF}, \lambda_{rej}}$	v3$_{TDCP_{Unc}, \lambda_{rej}}$
68 %	0.36	0.36	0.36	0.36	0.36	0.36
95 %	0.76	0.75	0.76	0.76	0.76	0.76
Normalized Exec Time	0.28	1.00	0.32	0.43	0.33	0.38

Table 2: IGS CDF results for all configurations.

2. Dynamic Datasets

The results were obtained using Dual Frequency observables on GPS (L1 C/A and L2) and Galileo (E1b + E5b). In the following sections, several configurations of the TDCP filter will be evaluated: with both Cycle Slip methods presented in III.3, Iono-free TDCPs and uncombined TDCPs. The full results will be presented in tables while the CDFs of the ambiguity estimating filter and only of the best performing TDCP filter will be presented for the sake of readability.

a) Open-Sky

Figures 7, 8, and 9 depict the CDF and estimated trajectory of the receiver with respect to the SPAN reference trajectory. It can be seen that the gain in accuracy in the TDCP filter with respect to the carrier based filter is small –11% for 68% of the time and a 17% gain in the y axis. This gain can be explained by the bridges (at around 180 seconds and 300 seconds) encountered during the data collect. Indeed, these bridges cause a temporary loss of lock leading to cycle slips in the carrier phase measurements. As this carrier filter does not perform cycle slip repair, the ambiguity must be re-estimated. This means that the benefit of using the accuracy of the carrier phase measurements is non-existent for that period of time. As a matter of fact, while the ambiguities are re-converging, the precision of the filter can even be degraded as is the case after the bridges. On the other hand, the TDCP appears to re-converge slightly faster after cycle slips. This is due to both the lack of ambiguity estimation and that the main positioning source comes from the pseudoranges.

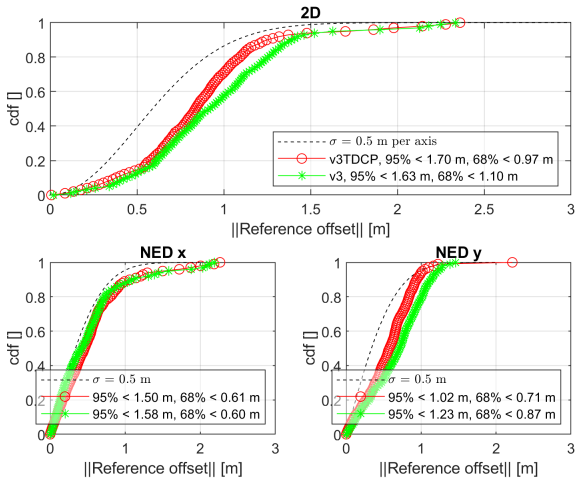

Figure 7: Highway CDFs.

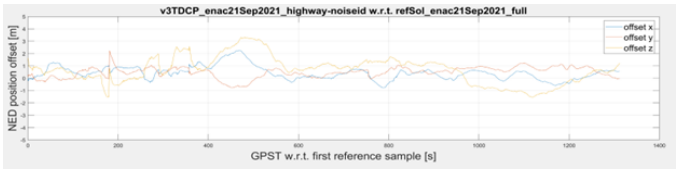

Figure 8: Highway Time series v3TDCP.

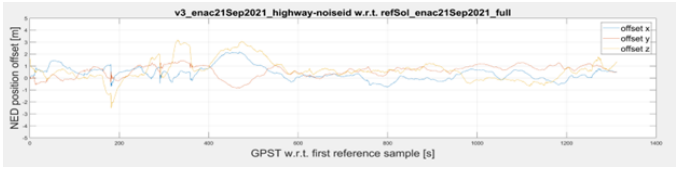

Figure 9: Highway Time series v3.

	v2	v3	v3$_{TDCP_{IF}, I_{rej}}$	v3$_{TDCP_{Unc}, I_{rej}}$	v3$_{TDCP_{IF}, \lambda_{rej}}$	v3$_{TDCP_{Unc}, \lambda_{rej}}$
68 %	1.00	1.10	0.98	0.97	0.99	1.01
95 %	1.70	1.63	1.70	1.70	1.71	1.73
Normalized Exec Time	0.33	1.00	0.48	0.57	0.41	0.57

Table 3: Highway CDF results for all configurations.

The results from table 3 highlight that in open-sky conditions, even in a dynamic scenario, the precision of the TDCP filter is dictated by the code and Doppler observables. Indeed, the accuracy of the code and Doppler (v2) filter is very similar to the one of the TDCP filters. The difference in accuracy is not big enough to claim, in this case, an added value from the TDCPs. Furthermore, the different configurations on the TDCP filter do not provide any significant difference between the configurations. This conveys a limited use of the TDCP measurements in low obstructed environments.

b) Sub-urban

The results from this data collect are presented in figures 10, 11, 12, and table 4. On this dataset, the Iono-free TDCP filter with Innovation based rejection is slightly outperformed by the ambiguity estimation filter on the y axis but their performance remain similar. Even though the receiver was in a sub-urban environment, there were only two signal obstructing moments (around 350s and 420s). The first occurrence was smoothed out by the TDCP filter as highlighted by Figure 11. This spike contained

in the carrier estimation filter is also present in the v2 filter. This implies that this comes from the code measurements which are likely affected by multipath. On the second obstruction, the TDCP filter does not outperform the v3 filter. For most of the obstruction, there were no visible satellite; hence, there were almost no GNSS observations. The accuracy of the filter then solely relies on the Inertial Measurement Unit.

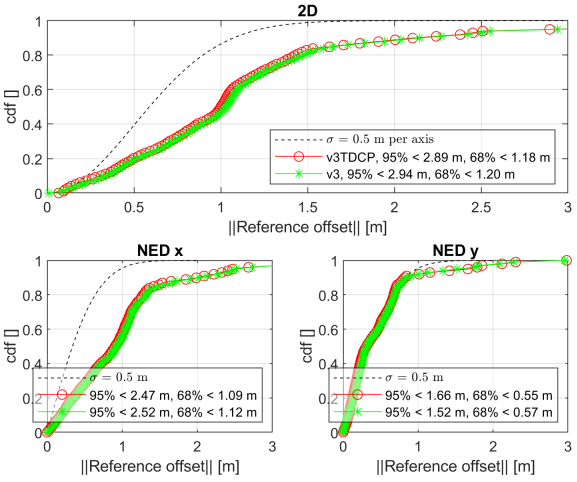

Figure 10: Sub-Urban CDFs.

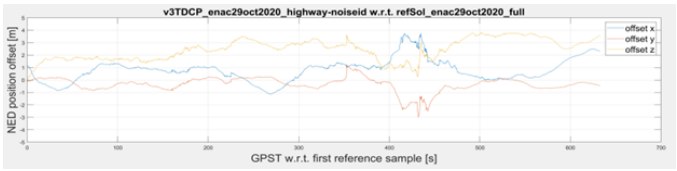

Figure 11: Sub-Urban Time series v3TDCP.

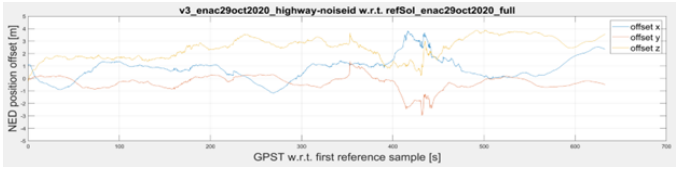

Figure 12: Sub-Urban Time series v3.

	v2	v3	v3$_{TDCP_{IF}, I_{rej}}$	v3$_{TDCP_{Unc}, I_{rej}}$	v3$_{TDCP_{IF}, \lambda_{rej}}$	v3$_{TDCP_{Unc}, \lambda_{rej}}$
68 %	1.21	1.20	1.18	1.18	1.19	1.18
95 %	3.11	2.94	2.89	3.05	2.92	3.01
Normalized Exec Time	0.25	1.00	0.34	0.36	0.44	0.58

Table 4: Sub-urban CDF results for all configurations.

For this scenario, the TDCP filter provides a marginal gain with respect to the carrier phase measurement. The benefit of TDCP measurements in suburban environments is that it matches the performance of a simple ambiguity estimation process while being 66% faster. Furthermore, the code and Doppler only filter is outperformed by 7% in 95% of the time by the TDCP filter. This further highlights that TDCPs can help smooth out the solution when obstacles are present. In table 4, it is shown that the filters processing Ionosphere-free TDCPs outperform the uncombined TDCP based filters. As illustrated by the histograms of the innovations, the uncombined TDCPs can be affected by a remaining ionospheric bias on top of cycle slips. Thus, if not correctly excluded, these measurements mitigate the benefit of TDCP measurements.

c) Deep Urban

As highlighted by Figure 13, the Iono-free TDCP filter with Innovation based rejection brings a significant positioning improvement in deep urban conditions with respect to the ambiguity filter. As shown by figure 14 and 15, the time series of the TDCP filter is much smoother thanks to the lack of ambiguity estimation. Indeed, this frequent reset in the EKF, due to cycle slips, leads to position uncertainty. This scenario demonstrates that TDCP measurements are most useful in heavily obstructed environments. During cycle slips, TDCP measurements are only excluded for that epoch and then the filter goes back to "normal" as the position increments are computed. On top of this accuracy gain of 11%, the filter is on average 66% faster (in MATLAB) than the ambiguity estimating filter. Finally, the TDCP filter is 39% and 52% more accurate for 68% and 95% of the epochs respectively than the v2 filter while only taking 25% longer per epoch. This illustrates the perks of including TDCPs in the filter as the environment of the receiver becomes more obstructed.

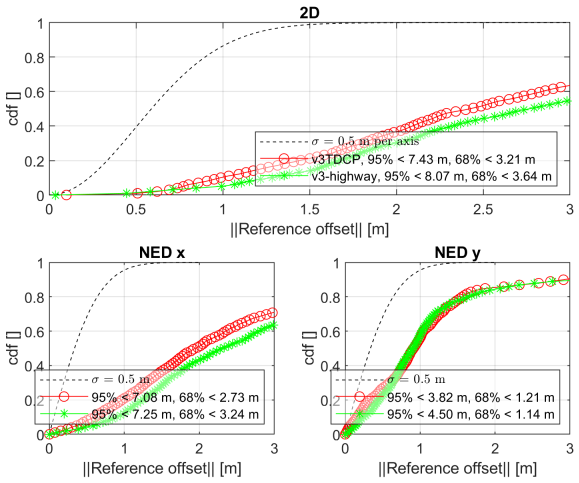

Figure 13: Urban CDFs.

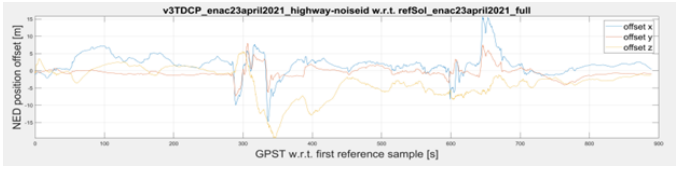

Figure 14: Urban Time series v3TDCP.

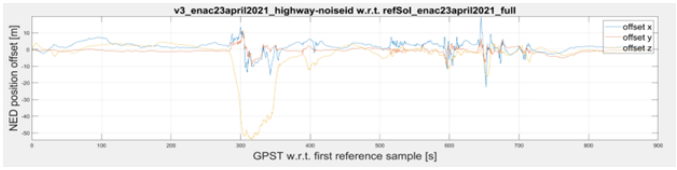

Figure 15: Urban Time series v3.

	v2	v3	$v3_{TDCP_{IF}, I_{rej}}$	$v3_{TDCP_{Unc}, I_{rej}}$	$v3_{TDCP_{IF}, \lambda_{rej}}$	$v3_{TDCP_{Unc}, \lambda_{rej}}$
68 %	5.21	3.64	3.21	3.31	4.74	3.72
95 %	15.52	8.07	7.43	11.60	25.50	9.17
Mean Exec Time (s)	0.26	1.00	0.33	0.43	0.46	0.47

Table 5: Urban CDF results for all configurations.

Table 5 further highlights that the TDCP filter can outperform v3. However, it also demonstrates that the tuning of the filter is very important. There is a big positioning discrepancy between the filter using Ionosphere-free TDCPs and excluding them with Innovation Monitoring and the one based on wavelength difference. When excluding Iono-free TDCPs with the latter, the wavelength of the combined measurement is reduced as shown by equation 31.

$$\lambda_{IF} = c\frac{f_1 - f_2}{f_1^2 - f_2^2} \tag{31}$$

Where:

- f_1 is the frequency of the first signal (in Hz)
- f_2 is the frequency of the second signal (in Hz)
- λ_{IF} is the wavelength of the first order iono-free combination signal

For GPS L1 C/A, its signal has a wavelength of approximately 19 cm while the iono-free combination of GPS L1 C/A and GPS L2 has a wavelength of around 10cm. So, by factoring the shorter wavelength and the increased noise due to the combination [Salós et al., 2010], the method presented in II.3.b becomes even more stringent. This leads to a high rejection of TDCPs (15% vs 1%), most of which are not affected by cycle slips and thus a very degraded solution.

The problem is the other way round for the uncombined TDCP filters. The histograms of the innovations (for the iono-free and uncombined filters with Innovation based rejection) depict that the uncombined TDCPs have a 13% higher standard deviation. The noise of uncombined signals is theoretically lower; thus, this implies that a remaining ionospheric component can affect some TDCPs, leading to position degradation if not correctly excluded. The lambda based rejection method is stricter as it rejects 14% of uncombined TDCPs, it rejects more "Iono affected" TDCPs and cycle slips inducing better results in deep urban environments.

VI. CONCLUSION

In this paper, an Extended Kalman Filter was designed which fuses code, Doppler, and Time Differenced Carrier Phase measurements with a low-cost IMU. The TDCPs effectively eliminate the tedious ambiguity estimation process in the absence

of cycle slips. The benefit of using TDCPs was studied in open-sky, sub-urban and deep urban scenarios. As the environment becomes more obstructed, cycle slips happen more regularly. Hence, two methods were proposed to detect and reject cycle slip affected TDCPs.

The results presented illustrate a correlation between the benefit of using TDCP measurements and how obstructed the environment is. Indeed, the TDCP filter provided a 7% improvement in sub-urban conditions with respect to a code and Doppler filter and a 11% improvement in deep urban conditions with respect to a filter using ambiguity estimation. The other perk of the proposed filter is its computational speed with respect to a regular ambiguity estimation filter. It is on average 66% faster.

The results convey that this TDCP filter can be a viable alternative to still make use of carrier phase measurements in solutions that target a low computational load. However, a special attention must be paid to the tuning of the filter as it was also shown that both cycle slip methods and the input TDCPs do not bring the same benefit. To avoid the risk of a Ionospheric bias remaining, iono-free TDCPs are preferred. Finally, the Innovation Monitoring rejection method to deal with Cycle slips is favored as it excludes less useful TDCP measurements.

As Global Navigation Satellite Systems (GNSS) continue to expand, there is an increase in the number of available signals. Indeed, Galileo is introducing Galileo E6, on top of the already existing signals (E1, E5a, and E5b). Meanwhile, GPS continues to transition its satellites to being L5 capable. Furthermore, Beidou has also become triple frequency capable [Chu and Yang, 2018]. In challenging GNSS conditions, such as urban canyons, the addition of new signals and constellations almost systematically improves the positioning accuracy, convergence or availability [Li, 2018] [Li, 2020]. Hence, the proposed filter could add triple frequency capabilities on the code and/or TDCP measurements. To keep the filter computationally lightweight, a simple combination as the one proposed in [Deo and El-Mowafy, 2016] could be implemented.

REFERENCES

[Bisnath, 2000] Bisnath, S. (2000). Efficient, automated cycle-slip correction of dual-frequency kinematic gps data. *Proceedings of ION GPS*, 23:145–154.

[Blewitt, 1990] Blewitt, G. (1990). An automatic editing algorithm for gps data. *Geophysical Research Letters*, 17(3):199–202.

[Brown, 2012] Brown, R. G. (2012). *Introduction to Random Signals and Applied Kalman Filtering with Matlab Exercises, 4th Edition*. American Institute of Aeronautics and Astronautics.

[Chu and Yang, 2018] Chu, F.-Y. and Yang, M. (2018). Beidou system (bds) triple-frequency ambiguity resolution without code measurements. *Remote Sensing*, 10:675.

[Deo and El-Mowafy, 2016] Deo, M. and El-Mowafy, A. (2016). Triple-frequency gnss models for ppp with float ambiguity estimation: performance comparison using gps. *Survey Review*, pages 1–13.

[Du and Gao, 2012] Du, S. and Gao, Y. (2012). Inertial aided cycle slip detection and identification for integrated ppp gps and ins. *Sensors (Basel, Switzerland)*, 12:14344–62.

[Duong, 2019] Duong, V. (2019). An optimal linear combination model to accelerate ppp convergence using multi-frequency multi-gnss measurements. *GPS Solutions*, 23.

[Gao et al., 2017] Gao, Z., Zhang, H., Ge, M., Niu, X., Shen, W., Wickert, J., and Schuh, H. (2017). Tightly coupled integration of multi-gnss ppp and mems inertial measurement unit data. *GPS Solutions*, 21:377–391.

[Groves, 2008] Groves, P. (2008). *Principles of GNSS, Inertial, Multisensor Integrated Navigation Systems*. Artech House.

[Kai et al., 2021] Kai, C., Chang, G., Chao, C., and Zhu, T. (2021). Improved tdcp-gnss/ins integration scheme considering small cycle slip for low-cost land vehicular applications. *Measurement Science and Technology*, 32.

[Kaplan, 2017] Kaplan, E. (2017). *Understanding GPS/GNSS principles and applications*. Artech House.

[Kim and Langley, 2001] Kim, D. and Langley, R. (2001). Instantaneous real-time cycle-slip correction of dual-frequency gps data.

[Kim et al., 2020] Kim, J., Park, M., Bae, Y., Kim, O.-J., Kim, D., Kim, B., and Kee, C. (2020). A low-cost, high-precision vehicle navigation system for deep urban multipath environment using tdcp measurements. *Sensors*, 20(11).

[Li, 2018] Li, B. (2018). Review of triple-frequency gnss: ambiguity resolution, benefits and challenges. *The Journal of Global Positioning Systems*, 16.

[Li, 2019] Li, P. (2019). Kalman-filter-based undifferenced cycle slip estimation in real-time precise point positioning. *GPS Solutions*, 23.

[Li, 2020] Li, P. (2020). Gps+galileo+beidou precise point positioning with triple-frequency ambiguity resolution. *GPS Solutions*, 24.

[Neyman and Pearson, 1933] Neyman, J. and Pearson, E. S. (1933). On the problem of the most efficient tests of statistical hypotheses. *Philosophical Transactions of the Royal Society of London. Series A, Containing Papers of a Mathematical or Physical Character*, 231:289–337.

[Park and Kee, 2010] Park, B. and Kee, C. (2010). The compact network rtk method: An effective solution to reduce gnss temporal and spatial decorrelation error. *Journal of Navigation*, 63(2):343–362.

[Parkinson, 1996] Parkinson, B. W. (1996). *Global Positioning System: Volume 1 Theory and Applications*. American Institute of Aeronautics and Astronautics.

[Rahman et al., 2015] Rahman, G., Mubeen, S., and Rehman, A. (2015). Generalization of chi-square distribution. *Journal of Statistics Applications Probability*, 4:119–126.

[Salós et al., 2010] Salós, D., Macabiau, C., Martineau, A., Bonhoure, B., and Kubrak, D. (2010). Nominal GNSS pseudorange measurement model for vehicular urban applications. In *IEEE/ION PLANS 2010, Position Location and Navigation Symposium*, pages pp 806–815, Indian Wells, United States.

[Soon et al., 2008] Soon, B., Scheding, S., Lee, H., Lee, H. K., and Durrant-Whyte, H. (2008). An approach to aid ins using time-differenced gps carrier phase (tdcp) measurements. *GPS Solutions*, 12:261–271.

[Tanil, 2022] Tanil, C. (2022). Kalman filter partial innovation sequence monitor. pages 1263–1272.

[Teunissen, 2006] Teunissen, P. J. G. (2006). The lambda method for the gnss compass.

[Vana et al., 2019] Vana, S., Naciri, N., and Bisnath, S. (2019). Low-cost, dual-frequency ppp gnss and mems-imu integration performance in obstructed environments. pages 3005–3018.

[Welch and Bishop, 1997] Welch, G. and Bishop, G. (1997). Scaat: Incremental tracking with incomplete information. pages 333–344.

[Zhu, 1994] Zhu, J. (1994). Conversion of earth-centered earth-fixed coordinates to geodetic coordinates. *IEEE Transactions on Aerospace and Electronic Systems*, 30(3):957–961.